

# vPET-ABC: Fast Voxelwise Approximate Bayesian Inference for Kinetic Modeling in PET

Qinlin Gu\* *Student Member, IEEE*, Gaelle M. Emvalomenos\*, Evan D. Morris, Clara Grazian, Steven R. Meikle *Senior Member, IEEE*

**Abstract**—Dynamic PET kinetic modeling increasingly demands voxelwise uncertainty quantification and robust model selection. Yet total-body PET (TB-PET) data volumes make conventional Bayesian approaches, such as per-voxel MCMC, computationally impractical, while deep models typically require retraining and careful revalidation when tracers, protocols, or kinetic models change, without necessarily improving inference speed.

Vectorized voxelwise approximate Bayesian computation (vPET-ABC) is introduced as a likelihood-free, model-agnostic posterior inference framework for dynamic PET kinetic modeling at total-body scale. The method replaces explicit likelihood evaluation with forward simulations and a discrepancy test, then exploits full vectorization to transform voxelwise inference into an embarrassingly parallel workload suited to modern GPUs.

In simulation, vPET-ABC produced posterior summaries with small divergence from sequential Monte Carlo baselines, and posterior mean estimates significantly more accurate than non-negative least squares (NNLS). For model selection between the linear parametric neurotransmitter model (lp-ntPET) and the multilinear reference tissue model, vPET-ABC maintained high sensitivity under high noise with moderate loss of specificity, whereas NNLS + Bayesian information criteria exhibited the opposite trade-off with near-zero sensitivity. In a proof-of-concept human cigarette smoking dataset, vPET-ABC yielded denser probabilistic activation maps than lp-ntPET with effective number of parameters. On a proof-of-concept 50 min total-body [<sup>18</sup>F]FDG study, vPET-ABC generated whole volume  $K_i$  parametric images within practical runtimes on a single data-center GPU. The results aligned with PET SUV, handled voxels violating irreversibility, and preserved local spatial correlation better than NNLS.

Overall, vPET-ABC delivers fast, training-free, uncertainty-aware inference that scales to TB-PET and remains portable across tracers and kinetic models.

**Index Terms**—Approximate Bayesian computation (ABC), CUDA, model selection, parametric imaging,

\* Q. Gu and G. M. Emvalomenos contributed equally to this work.

This work is supported by the Australian Research Council (Discovery Projects grant DP230102070).

Qinlin Gu (qinlin.gu@sydney.edu.au) is with the School of Mathematics and Statistics and the Brain and Mind Centre, the University of Sydney, Australia.

Gaelle M. Emvalomenos is with Radiology and Biomedical Imaging, Yale University, USA.

Evan D. Morris is with Radiology and Biomedical Imaging, Biomedical Engineering, and Psychiatry, Yale University, USA.

Clara Grazian is with the School of Mathematics and Statistics and the ARC Training Centre in Data Analytics for Resources and Environments (DARE), the University of Sydney, Australia.

Steven R. Meikle is with the School of Health Sciences, Sydney Imaging and the Brain and Mind Centre, the University of Sydney, Australia.

total-body PET, uncertainty quantification

## I. INTRODUCTION

WHEN applied to dynamic PET, kinetic modeling enables noninvasive quantification of physiological and molecular processes from time-activity curves (TACs) [1]. It describes radiotracer transport, tissue uptake and target engagement using compartmental models in the form of ordinary differential equations. This general methodology can be applied to a wide range of clinical and preclinical applications ranging from neurotransmitter studies in the neuroscience of addiction to tumor characterization in oncology [1]. Reliable estimation and inference are therefore central to PET quantification.

Total-body PET (TB-PET) is a recent advance whereby the axial field-of-view of the scanner is extended to 1 to 2 meters, resulting in ultra-high sensitivity [2], which improves signal-to-noise relative to injected dose and enables simultaneous whole-body kinetic analysis. However, it also introduces a model-selection challenge due to the wide variation in tracer kinetic behavior throughout the body and imposes a prohibitive computational burden for voxelwise parameter and uncertainty estimation at scale [3]. Against this backdrop, we summarize existing approaches and the practical trade-offs that shape current PET kinetic analysis methods.

In total-body PET, fast semi-quantitative whole-body parametric imaging is often performed with Patlak graphical analysis [4] to obtain voxelwise  $K_i$  (net influx). However, standard Patlak relies on the assumption of irreversible trapping of the tracer which may be valid in some organs but not others, motivating generalized Patlak formulations [5]. Patlak-style methods also focus primarily on  $K_i$ , while full compartmental modeling can provide additional macro- and micro-kinetic parameters that enable multiparametric characterization in total-body applications [3].

Deterministic estimators, such as fast non-negative least squares (FNNLS), are widely used in PET compartmental modeling, especially in basis-function formulations of kinetic models [6]. Although simple and fast, least-squares basis-function approaches can be sensitive to observational noise and their accuracy depends on basis-function choice, which can reduce sensitivity and reliability in practice [7]. These limitations become especially consequential when the goal is not only parameter estimation but also deciding between competing kinetic models, since the decision is made under the same noise, identifiability, and constraint structure.

Bayesian approaches address these issues by providing a Monte Carlo approximation to the full posterior probability distribution, enabling a more complete picture of parameter uncertainty [8]. The feasibility of posterior estimation in dynamic PET has been demonstrated at the region of interest (ROI) level, including Bayesian neurotransmitter PET (b-ntPET) [7] implemented with Markov chain Monte Carlo (MCMC) based on the linear parametric neurotransmitter PET model (lp-ntPET) [9], and likelihood-free approximate Bayesian computation for PET kinetic modeling (PET-ABC) [10]. However, conventional Monte Carlo methods [11] are difficult to scale voxelwise due to sequential sampling and convergence variability, while recent deep generative approaches tend to be slow at inference time (approx. 1 min/TAC) and still typically require retraining and revalidation when the tracer, protocol, or model changes [12].

We, therefore, propose vectorized voxelwise approximate Bayesian computation for PET kinetic modeling (vPET-ABC), a fast, likelihood-free, model-agnostic posterior sampler. This method builds on our prior work on PET-ABC [10], [13] by leveraging parallel simulation to deliver voxelwise posterior inference with calibrated uncertainty at whole-body scale.

In this study, we (i) formulate vPET-ABC for dynamic PET kinetic modeling and validate conditions under which vectorized, likelihood-free inference recovers accurate posteriors, (ii) provide a GPU-accelerated end-to-end pipeline from time activity curves (TACs) to posterior summaries that scales to whole-body volumes, (iii) evaluate the performance of vPET-ABC on two kinetic-model simulation benchmarks, assessing point-estimate accuracy, posterior fidelity, and model selection sensitivity, and (iv) demonstrate deployment in clinical studies without the requirement of training across tracers, models, and acquisition protocols. By combining likelihood-free Bayesian inference with vectorized computation, we show that vPET-ABC offers a practical, uncertainty-aware framework for large-scale kinetic parameter estimation aligned with contemporary TB-PET data volumes and hardware.

## II. METHODS

### A. Kinetic Models

Many kinetic models have been proposed over decades of research for a wide variety of tracers and molecular targets [14]. Here, we evaluate the performance and versatility of vPET-ABC in two distinct contexts: (i) assessing the reversibility or irreversibility of [<sup>18</sup>F]fluorodeoxyglucose (FDG) using the two tissue compartment model (2TCM), and (ii) analyzing stimulus-evoked neurotransmitter release in response to an external stimulus during scanning using the linearized parametric neurotransmitter PET model (lp-ntPET) [9] as in [15].

**1) Two Tissue Compartment Model:** The two-tissue compartment model [16] represents tracer kinetics with a plasma input  $C_p$  and two tissue compartments in series: free tracer  $C_f$  and metabolized tracer  $C_m$ . Compartment exchange is governed by non-negative rate constants  $K_1$  (plasma  $\rightarrow$   $C_f$ ),  $k_2$  ( $C_f \rightarrow$  plasma),  $k_3$  ( $C_f \rightarrow C_m$ ), and  $k_4$  ( $C_m \rightarrow C_f$ ), with  $k_4 = 0$  indicating irreversible trapping. The dynamics

are described by

$$\begin{aligned} \frac{dC_f}{dt} &= K_1 C_p - (k_2 + k_3) C_f + k_4 C_m, \\ \frac{dC_m}{dt} &= k_3 C_f - k_4 C_m, \end{aligned} \quad (1)$$

and the measured PET activity is

$$C_t(t) = (1 - V_b)(C_f(t) + C_m(t)) + V_b C_{wb}(t), \quad (2)$$

where  $V_b \in (0, 1)$  is the blood volume fraction and  $C_{wb}$  is whole-blood activity. In the irreversible case ( $k_4 = 0$ ), the model conforms to the Patlak linearization [4], although reversibility can be tissue-dependent [5]. For [<sup>18</sup>F]FDG, we assume  $C_p \approx C_{wb}$ .

**2) Linear Parametric Neurotransmitter PET model:** The lp-ntPET model [9] is a reference-tissue based non-steady state model for detecting transient task- or drug-evoked neurotransmitter changes without arterial sampling. It extends the multilinear reference tissue model (MRTM) [17] by adding a time-varying activation term that captures transient ligand displacement, typically parameterized using a basis set spanning a range of plausible onset, peak, and decay profiles. The linearized form is

$$C_t(t) = R_1 C_r(t) + k_2 \int_0^t C_r(u) du - k_{2a} \int_0^t C_t(u) du - \gamma B(t), \quad (3)$$

with

$$B(t) = \int_0^t C_t(u) g(u) du, \quad (4)$$

where  $C_r(t)$  is the reference-region TAC,  $R_1 = \frac{K_1}{K_1'}$  is the relative tracer delivery to target vs. reference,  $k_2$  is the target-tissue efflux rate constant (tissue  $\rightarrow$  plasma),  $k_{2a} = \frac{k_2}{1 + B P_{ND}}$  is the apparent efflux rate constant that incorporates specific binding, and  $g(t)$  is a gamma-variate activation profile [9]. Setting  $\gamma = 0$  reduces the model to MRTM, so lp-ntPET can be viewed as a generalization of MRTM.

### B. Bayesian Statistics

In kinetic modeling, Bayes' rule updates beliefs about parameters (e.g.,  $\boldsymbol{\theta} = (R_1, k_2, k_{2a}, \dots)^T$ ) given observed TACs  $\mathbf{C}$  (e.g.,  $\{C_t(t_i)\}_{i=1}^n$  and optionally  $C_r(t)$ ):

$$\pi(\boldsymbol{\theta} | \mathbf{C}) = \frac{p(\mathbf{C} | \boldsymbol{\theta}) \pi(\boldsymbol{\theta})}{p(\mathbf{C})} \propto p(\mathbf{C} | \boldsymbol{\theta}) \pi(\boldsymbol{\theta}). \quad (5)$$

Model selection introduces a discrete variable  $m \in \{1, \dots, M\}$  indexing candidate kinetic models, giving

$$\begin{aligned} \pi(m, \boldsymbol{\theta} | \mathbf{C}) &\propto p(\mathbf{C} | \boldsymbol{\theta}, m) \pi(\boldsymbol{\theta} | m) \pi(m), \\ \pi(m | \mathbf{C}) &= \int \pi(m, \boldsymbol{\theta} | \mathbf{C}) d\boldsymbol{\theta}. \end{aligned} \quad (6)$$

When the likelihood function  $p(\mathbf{C} | \boldsymbol{\theta})$  is tractable and a known noise model exists, Monte Carlo-based simulation methods are adopted to approximate the posterior distribution in Eq. (6).

As an alternative, approximate Bayesian computation (ABC) [18] provides likelihood-free Bayesian inference by replacing explicit likelihood evaluation with forward simulations and a discrepancy criterion, enabling posterior approximation and model selection under suitable conditions.

### C. Approximate Bayesian Computation and vPET-ABC

1) *Approximate Bayesian Computation*: One of the simplest ABC algorithms is the rejection sampling [19] method, which approximates the likelihood function by:

$$p(\theta | S(\mathbf{x}_{obs})) = \lim_{h \rightarrow 0} \int_{\mathbf{X}} p(\theta, \mathbf{x} | \rho(S(\mathbf{x}), S(\mathbf{x}_{obs}) \leq h) d\mathbf{x}, \quad (7)$$

where  $\mathbf{x} \in \mathbf{X}$  are simulated data,  $\mathbf{x}_{obs} \in \mathbf{X}$  are observed data,  $\rho(\cdot)$  is a distance function,  $S(\cdot)$  is a (possibly sufficient) summary statistic to reduce the dimensionality and computation required, and  $h$  is the acceptance threshold.

For each voxel, rejection ABC repeatedly samples a candidate model and its parameters from the prior, simulates a TAC, and accepts the draw if the discrepancy between simulated and observed summary statistics is below a tolerance  $h$ . This is repeated until  $n$  draws are accepted.

2) *vPET-ABC*: *vPET-ABC*: The conventional ABC algorithm can also be implemented under a fixed simulation budget  $N$  (i.e., a fixed computational budget or total number of simulations). Instead of running the algorithm until  $n$  draws with distances below the threshold  $h$  have been accepted, one performs  $N$  simulations and retains the closest  $p = n/N$  proportion of simulated distances, following Biau *et al.* [20].

For ease of parallelization and vectorization to enable large-scale voxelwise PET kinetic modeling, we further adapted the conventional ABC algorithm in a PET kinetic modeling context to be fully compatible with matrix calculations for ease of GPU implementation, as shown in Alg. 1. We will show in the next section that through vectorization and the utilization of modern GPUs, we mitigate ABC's low acceptance/space-exploration efficiency in comparison with MCMC or sequential Monte Carlo (SMC), achieving speed comparable to FNNLS. We will also show that such adaptation does not retard convergence rate.

---

**Algorithm 1:** Vectorized Voxelwise Rejection ABC algorithm (vPET-ABC),  $M$  is the number of models,  $P$  is the number of parameters,  $N$  is the simulation size,  $J$  is the number of voxels,  $p = \frac{\hat{n}}{N}$  is the proportion of accepted samples where  $\hat{n}$  is the desired accepted number of samples,  $L$  is the number of frames for each TAC.

---

Sample model indicators  $m \in \mathbf{M} = \{0, 1, \dots, M - 1\}$  with equal probability of  $\frac{1}{M}$ ;

Sample model parameters, stored together in a matrix  $\Theta$  of shape  $(N, P + 1)$  together with the model indicators;

Compute model curves using  $\Theta$ , stored in a matrix  $\mathbf{X}$  of shape  $(N, L)$ ;

Compute distances on summary statistics  $\rho(S(\mathbf{X}), S(\mathbf{x}_{obs}))$ , stored in a matrix  $\mathbf{D}$  of shape  $(J, N)$ ;

Compute the smallest  $p$  proportion along the  $N$  dimension in  $\mathbf{D}$ , as the accepted posteriors of all voxels with a shape of  $(J, \hat{n})$ ;

---

Fixing  $p$  in Alg. 1 is equivalent to fixing  $n$ , the accepted number of samples, if  $p \in [\frac{n}{N}, \frac{n+1}{N})$  such that  $n = \lfloor \hat{N}p \rfloor$  still holds.

### D. Optimizations and Usage Pipeline

This section outlines key ABC components and how to tune them, and presents a practical user-facing pipeline.

1) *Summary Statistic  $S(\cdot)$* : In Fan *et al.* [21], two alternative summary statistics were evaluated: the raw (noisy) observed TAC and a smoothing-spline estimate of the TAC. They observed that both performed well at low noise capturing the true curve within the 95% credible interval, while the spline summary was more robust under higher noise. To mitigate the computational burden of smooth spline estimations in large datasets, we recommend using the observed TAC as the summary statistic.

2) *Threshold  $h$* : The proportional threshold  $p$  (acceptance rate) controls the bias–variance trade-off of ABC estimators and also affects model-selection sensitivity/specificity. Tuning hyperparameters  $h, p, n$  is challenging, but here we propose a method inspired by Barber *et al.* [22].

Tuning  $h, p, n$  for parameter accuracy, we recommend a short pilot on simulation data matched in parameter ranges and noise, where the true parameter values are known: (i) for a small grid of  $n$  values, compute the posterior mean of a target parameter across repetitions and estimate its MSE; (ii) for sufficiently small  $h$ , the MSE versus  $h$  or  $n$  curve is U-shaped; (iii) fit a smooth curve and identify the value corresponding to the minimum of the fitted curve.

Tuning  $h, p$ , and  $n$  for model selection requires a different calibration. Under a fixed simulation budget, ABC may intrinsically penalize more complex models because their higher-dimensional parameter spaces are explored less thoroughly. By contrast, NNLS-based model selection typically relies on explicit criteria such as information criteria or  $F$ -tests, while ABC offers a coherent simulation-based approach to model comparison when likelihood-based criteria are unavailable or unreliable. Although recent theory for ABC model selection is available [23], it relies on assumptions that are not satisfied in our kinetic modeling setting. We therefore recommend the following empirical calibration pipeline: (i) simulate datasets from each candidate model at representative parameter/noise settings; (ii) vary  $n$  (or  $p$ ) over a prespecified grid and compute accuracy and ROC AUC for each model; (iii) choose a working point in the elbow-shaped curve that achieves the desired balance between sensitivity and specificity across models.

3) *Point Estimate and Other Inference Questions*: In medical imaging, a common output is a parametric map that enables an informative visualization of the kinetic modeling result. In order to obtain these images, one value per voxel is required, which is generally a frequentist point estimate. In a Bayesian setting, in order to create a parametric map, a point estimate can be the posterior mean, the geometric median or the Minimum Mean Square Error (MMSE) applied to the Highest Posterior Density (HPD) of a region [7]. Given the theoretical guarantees and computational simplicity, we recommend the posterior mean; HPD can be tricky and computationally demanding for ABC since it requires density estimation (e.g., KDE) on accepted samples.

The strength of Bayesian analysis, however, lies in quantifying uncertainty via the posterior distribution. In a 1p-ntPET model study, for instance, when it is difficult to decide the

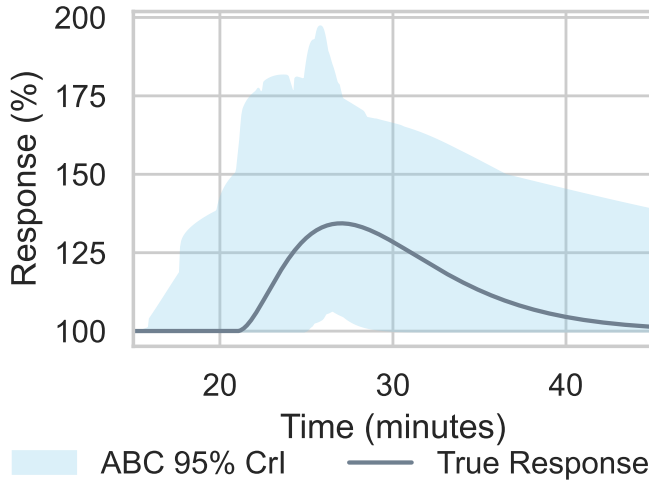


Fig. 1. 95% credible interval of the response function  $k_{2a}(t)/k_{2a} = 1 + \gamma/k_{2a} \cdot g(t)$  in the lp-ntPET model, expressed as percentage above baseline.

presence or absence of significant neurotransmitter activation, Bayesian credible interval (CrI) of the response function  $\frac{k_{2a}(t)}{k_{2a}} = 1 + \frac{\gamma}{k_{2a}}g(t)$  provides additional insight to inform the decision. In the example of Fig. 1, we can infer activation since the lower bound of the ABC 95% CrI excludes a flat (null) response.

### III. EXPERIMENTS

The proposed method and pipelines were applied and evaluated on several simulation and real datasets. The two tissue compartment model simulation was used to test kinetic parameter point estimate accuracy, while the lp-ntPET/MRTM simulation was chosen to validate kinetic parameter posterior distribution accuracy, speed performance, and most importantly model selection sensitivity. Two real datasets were then selected to showcase how the method should be applied in practical cases and how well they perform compared with established non-Bayesian approaches.

#### A. Simulation datasets

1) *Two Tissue Compartment Model*: Ten thousand 1D 2TCM TACs were simulated from Eq. (1) and Eq. (2) using kinetic parameters  $(K_1, k_2, k_3, k_4, V_b)$  sampled uniformly from ranges reported in the PET literature for  $[^{18}\text{F}]\text{FDG}$  in a wide variety of organs and tissues [24], [25]. Specifically, we chose

$$\begin{aligned} K_1 &\in [0.001, 1.00] \text{ mL min}^{-1} \text{ cm}^{-3}, & k_2 &\in [0.001, 2.00] \text{ min}^{-1} \\ k_3 &\in [0.001, 0.50] \text{ min}^{-1}, & k_4 &\in [0, 0.10] \text{ min}^{-1} \\ V_b &\in [0.03, 0.20]. \end{aligned} \quad (8)$$

The arterial blood input function was simulated using Feng's model [26]:

$$C_a(t) = (\beta_1 t - \beta_2 - \beta_3)e^{-\kappa_1 t} + \beta_2 e^{-\kappa_2 t} + \beta_3 e^{-\kappa_3 t}, \quad (9)$$

where the six parameters  $(\beta_1, \beta_2, \beta_3, \kappa_1, \kappa_2, \kappa_3)$  were drawn uniformly from the following ranges:

$$\begin{aligned} \beta_1 &\in [4 \times 10^4, 4.7 \times 10^5], & \beta_2 &\in [1 \times 10^4, 2 \times 10^5], \\ \beta_3 &\in [8 \times 10^3, 3 \times 10^4], & \kappa_1 &\in [1, 1 \times 10^3], \\ \kappa_2 &\in [0.03, 3.60], & \kappa_3 &\in [0.01, 0.035], \end{aligned} \quad (10)$$

covering the full variability observed in eight oncological subjects aged 43-82 years (Mean $\pm$ SD: 70.53 $\pm$ 10.36), weighing 55-97 Kg (Mean $\pm$ SD: 71.23 $\pm$ 12.80 Kg) acquired on a Siemens Biograph Vision Quadra (Siemens Healthineers, Knoxville, TN). All subjects were administered  $[^{18}\text{F}]\text{FDG}$  as an intravenous bolus (Mean $\pm$ SD: 146.67 $\pm$ 11.50 MBq in 1.0 $\pm$ 0.5 ml at 10 ml/min).

Gaussian noise was then added to the simulated TACs,  $C_t$ , according to the model [10]:

$$y(t) = C_t(t) + \ell \sigma_t \mathcal{N}(0, 1), \quad (11)$$

where  $\sigma_t = \sqrt{\frac{C_t(t)\exp(-\lambda t)}{\Delta t}} \exp(\lambda t)$ .  $\Delta t$  is the duration of a given frame in the PET time series,  $\lambda = \ln 2/T_{1/2}$  is the decay constant for  $^{18}\text{F}$ , with  $T_{1/2} = 109.8$  min and  $\ell$  is a constant that scales the noise level. To match realistic noise levels,  $\ell = 7$  was estimated from the aforementioned eight PET scans using MCMC.

Standard least squares method (Trust Region Reflective algorithm implemented via `scipy.optimize.least_squares` using default arguments) and vPET-ABC ( $N = 10,000,000, n = 18$ ) were applied to the simulation dataset, and evaluated by comparison to ground truth.

2) *Linear Parametric Neurotransmitter PET model*: Two 1D simulation datasets at different noise levels, each containing 4000  $[^{11}\text{C}]\text{raclopride}$  TACs with 61 frames of 60 seconds duration, were generated using the neurotransmitter PET (ntPET) model [27] with the same parameters as from the literature [28]. Half included dopamine activation, indicated by non-zero  $\gamma$ , while the remainder had no activation ( $\gamma=0$ ). Gaussian and Poisson noise models were applied separately [10], each to 2000 TAC simulations:

$$\begin{aligned} \epsilon_{\text{Gaussian}} &\sim \mathcal{N}(0, l_1 \sqrt{\frac{C_T(t)}{\Delta t e^{\lambda t}}}), \\ \epsilon_{\text{Poisson}} &\sim \frac{\text{Pois}(l_2 C_T(t))}{l_2}, \end{aligned} \quad (12)$$

where  $l_1, l_2$  are the noise-level constants and  $\lambda = \ln \frac{2}{T_{1/2}}$  is the decay constant for the tracer. The two noise levels chosen correspond to noise observed on a microPET Focus 220 (Siemens Healthineers, Knoxville, TN) (high noise) and a Bruker Si78 (Bruker Biospin, Ettlingen, Germany) (low noise).  $l_1, l_2$  were estimated from real Bruker/microPET scans using an MCMC sampler under the corresponding noise model, and then used as constants for the simulation.

NNLS with basis functions [9], vPET-ABC, SMC [29] and Hamiltonian Monte Carlo (HMC) [30] were applied to the simulated datasets for further evaluation of computational speed, model selection sensitivity and kinetic parameter posterior accuracy.  $t_D, t_P$ , and  $\alpha$  were discretized onto predefined grids to construct the basis-function library. Specifically,  $t_D \in [15, 25]$

with unit increments; for each  $t_D, t_P \in [t_D + 1, t_D + 45]$  with unit increments; and  $\alpha \in 0.25, 1, 4$ , consistent with prior work [31].

## B. Proof-of-Concept Studies

1) *Human Cigarette Smoking Study*: To apply the vPET-ABC pipeline to real dynamic PET data for capturing stimulus-evoked neurotransmitter release, we followed the pipeline in Section II-D, beginning with realistic simulations to optimize  $n$  (desired number of accepted simulations) for model selection. We generated realistic 90-min TACs by creating a 4D human striatum phantom, as described by Liu and Morris [31], for which [ $^{11}\text{C}$ ]raclopride kinetics were simulated using COMKAT in Matlab (Mathworks) [32] with noise corresponding to the HRRT PET scanner (Siemens Healthineers, Knoxville, TN), then denoised with a  $3 \times 3 \times 3$  voxel HighY constrained backProjection (HYPR) filter [33], exactly matching the processing applied to real data. As in [31], a cerebellar reference-region TAC was simulated, along with striatal TACs spanning fast and slow kinetics: 1345 voxels with dopamine activation and 505 voxels without activation (NULL). Dopamine activation profiles were modeled as a gamma-variate scaled by magnitude  $G$ ,  $DA(t) = Gg(t) + \text{baseline}$ , where  $G$  is the peak DA increase above baseline and  $g(t)$  is the normalized DA signal defined in Eq.(4). All signals used  $G \in [50, 600]$  nM in 50 nM increments, with baseline DA set to 100 nM; hereafter we report  $G$  as percentage above baseline ( $G\%$ ) for ease of interpretability (see [31]).

In the activated voxels we chose similar values for the magnitude and timing parameters to those in [31] but lowered the magnitude of DA release in order to simulate more subtle responses:

$$\begin{aligned} \text{Low magnitude: } G &\sim \mathcal{N}(150\%, (20\%)^2), \\ \text{High magnitude: } G &\sim \mathcal{N}(350\%, (20\%)^2), \\ \text{Early peak time: } t_P &< 45 \text{ min}, \\ \text{Late peak time: } t_P &> 45 \text{ min}, \\ \text{Time of onset: } t_D &\sim \mathcal{U}[30, 40] \text{ min}, \\ &\alpha \sim \mathcal{N}(0.7, 0.1^2), \end{aligned} \quad (13)$$

As preparation for the experiment, we applied the vPET-ABC with  $N = 10,000,000$  simulations and with a decreasing number of accepted samples  $n \in \{200, 150, 100, 50, 25, 15\}$ . We calculated the sensitivity and specificity based on the percentage of correctly identified activated and NULL cases, respectively, overall as well as for the different sub-groups of activated cases (i.e. “low”, “high”, “early”, “late” and their different combinations). An optimal  $n$  (desired number of accepted simulations) for model selection was then determined for a further in-human study.

We then applied the vPET-ABC pipeline to a dynamic scan of a human subject smoker. Following 1 week under placebo patch as opposed to a nicotine patch and then overnight abstinence, the smoker participated in a 90-minute [ $^{11}\text{C}$ ]raclopride scan in the HRRT PET scanner (Siemens Healthineers, Knoxville, TN) and smoked a cigarette while in the scanner starting at 35 min post injection and lasting for

approximately 3 minutes. The study was approved by the Yale Human Investigation and Radiation Safety Committees. More details on the data acquisition can be found in Zakiniaiez *et al.* [34].

A 1004-voxel mask delineating the precommissural striatum and its subregions (ventral striatum, dorsal caudate, dorsal putamen), following Martinez *et al.* [35], was applied prior to kinetic analysis. Within this mask, we compared the number and location of voxels identified as activated by two time-varying methods: the lp-ntPET model with effective number of parameters (ENP), as described in [15], [36] and the proposed vPET-ABC method with parameters optimized in the aforementioned simulation. The lp-ntPET ENP method produces a binary map of activated voxels while vPET-ABC generates a map of probabilities for selecting lp-ntPET over MRTM (i.e. activation vs NULL).

2) *Human [ $^{18}\text{F}$ ]FDG TB-PET Study*: A 54 year old male subject with a pancreatic neuroendocrine tumour underwent a 50-min dynamic total-body PET scan on a Siemens Biograph Vision Quadra (Siemens Healthineers, Knoxville, TN) commencing with intravenous administration of 150 MBq of [ $^{18}\text{F}$ ]FDG. This scan was part of a larger study approved by the Northern Sydney Local Health District Human Research Ethics Committee. Prior written informed consent to participate in this study was obtained from the subject.

List-mode data were rebinned into 35 temporal frames (matrix size  $220 \times 220 \times 645$ ). Standard corrections (normalization, randoms, attenuation, decay, and scatter) were applied, and images reconstructed using ordinary-Poisson ordered-subsets expectation maximization (OP-OSEM; 8 iterations, 5 subsets) with time-of-flight weighting and a maximum ring difference of 322. Spatiotemporal HYPR filtering was then applied to the dynamic series [33], prior to kinetic modeling. The arterial input function was extracted from the ascending aorta: a 3D aortic mask was generated on the native CT using MOOSE segmentation [37] and eroded by two voxels to mitigate partial-volume contamination; whole-blood image-derived arterial input function (IDIF) values were defined as the frame-wise mean activity concentration within the eroded region.

vPET-ABC was then run on the dataset using the 2TCM with model selection for the presence or absence of reversibility (i.e.,  $k_4 = 0$  or  $k_4 \neq 0$ ) under wide prior distributions defined as:

$$\begin{aligned} K_1 &\sim \mathcal{U}(0.001, 1), & k_2 &\sim \mathcal{U}(0.001, 2), \\ k_3 &\sim \mathcal{U}(0.001, 0.5), & k_4 &\sim \mathcal{U}(0, 0.1), \\ V_b &\sim \mathcal{U}(0.03, 0.2), & m &\sim \text{Bern}\left(\frac{1}{2}\right), \end{aligned} \quad (14)$$

where  $\text{Bern}(p)$  stands for a Bernoulli distribution of parameter  $p$ .

The prior distributions were based on values reported in the literature for [ $^{18}\text{F}$ ]FDG in a wide variety of organs and tissues [38]–[40]. The simulation size  $N$  was selected to be sufficiently large but still fit within GPU memory and in reasonable time. The accepted number  $n$  was chosen to be an arbitrarily small number to minimize bias under fixed  $N$  but also not too small that Monte Carlo error is large.

Thus, we selected  $N = 10,000,000$  and  $n = 18$ . For more rigorous studies, we recommend that users optimize  $n$  with the guidance of a pilot study, as discussed in Section. II-D.

Point estimates of the kinetic parameters were calculated as the means of their respective posterior distributions conditioned on the preferred model for each voxel. A model is preferred when more than 50% of all  $n$  accepted simulations in a voxel is produced by the candidate model. Afterwards, a  $K_i$  parametric image was created by computing  $K_i = K_1 k_3 / (k_2 + k_3)$  based on accepted samples forming  $k_i$  posterior distributions, the mean estimator of which was then further compared with both a standard Patlak [4] image, and the standard SUV image as a clinical reference.

Local spatial autocorrelation preservation was assessed using local Moran's I on coronal 2D maps (SUV, Patlak  $K_i$ , NNLS  $K_i$ , and ABC  $K_i$ ). To remove large-scale spatial trends, each map was detrended by subtracting an anisotropic Gaussian-smoothed field with FWHM 40 mm. The corresponding kernel widths were converted using the in-plane voxel spacing ( $1.6456 \times 3.3$  mm). The detrended maps were then z-scored within a common mask. Local Moran's I was computed using an 8-neighbor, distance-weighted, row-standardized neighborhood. We summarized each method using the distribution of Moran's I values and the voxelwise correlations between Moran's I maps.

## IV. RESULTS AND DISCUSSION

### A. 2TCM Simulations

Fig. 2 shows distributions of log-ratio errors for all kinetic parameters, with each parameter binned by groups of true magnitude. Paired permutation tests indicate vPET-ABC performed significantly better in terms of log-ratio error of all kinetic parameters except  $k_3$  which was estimated equally well by either method. For larger kinetic parameter values, vPET-ABC showed smaller bias than NNLS.

NNLS methods impose assumptions such as predefined basis grids and passbands, non-negativity constraints and time-weighting, all of which act as implicit regularization and potentially lead to biased estimates [41]. This is not unique to 2TCM, as it is also evident in other methods such as lp-ntPET [9] where the regressor is correlated with the regression error. In practice, NNLS methods are sensitive to observational noise, reducing sensitivity to subtle parameter differences.

### B. lp-ntPET Simulations:

Table I compares runtime for four methods: NNLS+Basis Library, Monte Carlo baselines (SMC and HMC/NUTS) and vPET-ABC. vPET-ABC on GPUs achieves substantially lower runtime than SMC/HMC and is comparable to NNLS on CPUs, indicating effective use of accelerator hardware. In contrast, the GPU implementation of NNLS was slower than its CPU counterpart in our experiments, suggesting limited parallelization efficiency in this setting and less effective use of GPU hardware than vPET-ABC.

Fig. 3 depicts the accuracy of posterior distribution estimation by vPET-ABC relative to SMC which is treated as the ground truth. An arbitrary TAC was chosen for demonstration

TABLE I  
RUNTIME COMPARISON PER VOXEL

Method	Algorithm	PC <sup>e</sup> Time (s)		HPC <sup>f</sup> Time (s)	
		CPU	GPU	CPU	GPU
NNLS+Basis Library	FNNLS <sup>a</sup>	0.181	—	<0.0001	0.075
SMC	Independent MH <sup>b</sup>	58	—	—	—
HMC	NUTS <sup>c</sup>	137	16050	462	4928
ABC	vPET-ABC <sup>d</sup>	—	0.239	—	0.0065

<sup>a</sup> Fast Non-negative Least Squares [42] `scipy.optimize.nnls` for CPUs and `jaxfit.CurveFit` for GPUs. The basis library size was 1185; not vectorized.

<sup>b</sup> Independent Metropolis-Hastings, `pymc.smc.sample_smc`, 10,000 draws.

<sup>c</sup> No-U-Turn Sampler, `pymc.sampling.jax.sample_numpyro_nuts`, 5,000 burn-in and 10,000 draws.

<sup>d</sup> `vpetabc.ABCRejection`.

<sup>e</sup> Commodity PC, CPU: 12th Gen Intel(R) Core(TM) i7-12700H (2.30 GHz), GPU: NVIDIA GeForce RTX 3060 Laptop GPU. JAX does not support NVIDIA CUDA on Windows x64, all code run under Windows WSL2.

<sup>f</sup> NCI Gadi cluster, CPU: 24-core Intel Xeon Scalable 'Cascade Lake', GPU: NVIDIA V100.

TABLE II  
MODEL-SELECTION PERFORMANCE BY NOISE LEVEL

Method	Noise	Performance	
		Sensitivity <sup>a</sup>	Specificity
NNLS+Basis Library <sup>b</sup>	Low	0.843	0.994
ABC	Low	0.925	0.955
NNLS+Basis Library	High	0.102	0.996
ABC	High	0.880	0.575

<sup>a</sup> Positive = activation ( $\gamma \neq 0$  in lp-ntPET).

<sup>b</sup> NNLS+Basis Library model selection via Bayesian information criteria (BIC).

as all TACs are different noise realizations of the same physiologically feasible TAC. Convergence of the SMC posterior approximation was assessed using four independent SMC runs (`PyMC sample_smc, chains=4`). We evaluated between-run agreement using Gelman–Rubin  $\hat{R}$  and effective sample size (ESS) computed in ArviZ. All parameters had  $\hat{R} \leq 1.01$  (mode 1.00), with adequate ESS, indicating stable posterior estimates across independent SMC runs. Most vPET-ABC posteriors resemble those of SMC with small KL divergences, with the minor exception of  $R_1$  where SMC produced a posterior distribution with a narrower spread,  $t_D$  where SMC revealed a roughly monotonically decreasing distribution, and  $t_P$  where SMC identify an asymmetric distribution with a heavy upper tail.

For model selection sensitivity, ABC and NNLS with a basis library perform similarly at the lower noise level (Table II). At the higher noise level, ABC maintains higher sensitivity with moderate specificity. While NNLS model selection is often implemented via F-tests or information criteria (IC) [43], these approaches have well-known pitfalls in kinetic modeling. AIC penalizes model complexity using only the number of free parameters, whereas the effective complexity also depends on parameter identifiability (i.e., the local information of the likelihood) [44]. AIC is easily biased by boundary constraints [44], and often requires manual calibration to improve sensitivity [36]. Moreover, many IC are plug-in scores evaluated at point estimates, discarding posterior uncertainty [45], and even defining the effective sample size for penalization is non-trivial given temporally correlated TACs and implementation details

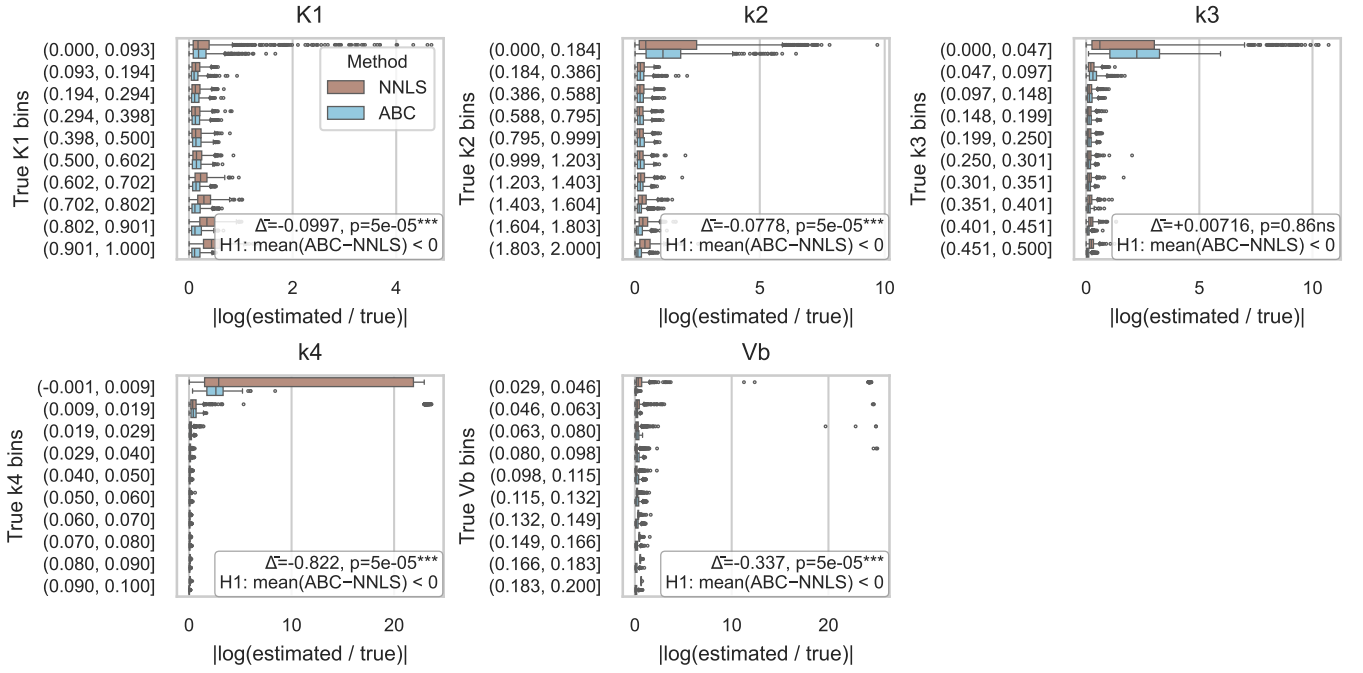


Fig. 2. Parameter point estimate accuracy comparison on the entire simulation set, comparing NNLS and vPET-ABC. The plot shows log-ratio error by true magnitude for all kinetic parameters. Paired permutation test results are shown in boxed inserts.

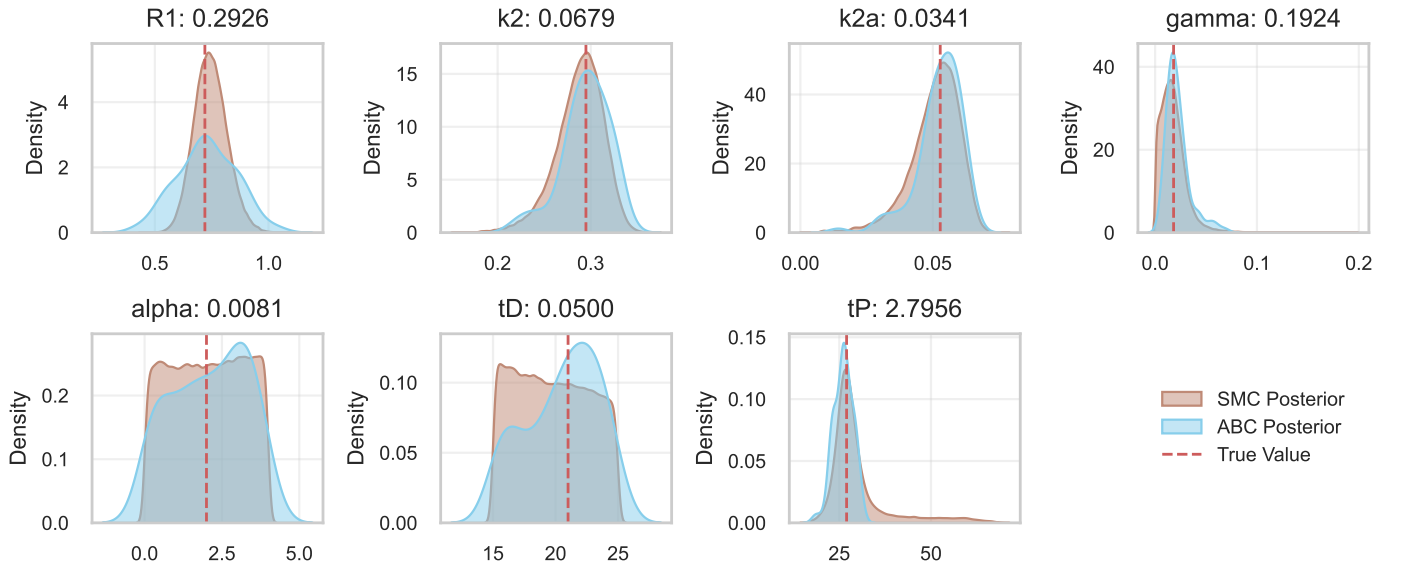


Fig. 3. Posterior distribution comparison between SMC and vPET-ABC on a TAC with activation. The values shown in each subplot title are the KL values:  $\text{KL}[\text{SMC} | \text{ABC}]$ . The red dashed vertical lines indicate true parameter values.

such as up-sampled convolution or basis-function parameterization [36]. Finally, the “linear” lp-ntPET formulation (Eq. (3)) includes a regressor  $\int_0^t C_T(u) du$  that can be correlated with noise, violating Gauss–Markov assumptions (notably strict exogeneity), so least-squares estimates may not be BLUE (best linear unbiased estimates) and may yield biased parameter estimates and model selection.

Note that, as our pilot run was intended to optimize ABC hyperparameters for better kinetic parameter accuracy, sub-optimal model selection accuracy was expected. For a study focusing on model selection (such as Section. III-B.1), a

different pilot study designed to optimize model sensitivity or specificity can improve the corresponding result further.

### C. Human Cigarette Smoking Study

In Table III, we report the percentage of correctly detected activated voxels and null voxels. For the null case, the percentage decreases as the number of accepted simulations ( $n$ ) is reduced, ranging from 99.5% to 89.2%. In contrast, for the activated voxels, the percentage increases over the same range, from 88.8% to 99.2%. Notably, the two percentages converge at 50 accepted simulations. Also, for the sub-categories of

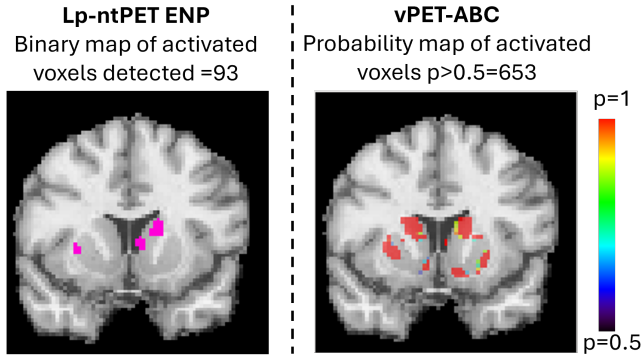


Fig. 4. Model selection maps from a human [ $^{11}\text{C}$ ]raclopride PET dataset co-registered to the MNI template. Left: binary lp-ntPET ENP map, where pink voxels indicate significant dopamine activation. Right: vPET-ABC activation probability map, with higher probabilities ( $p \in [0.5, 1]$ ) indicating stronger evidence for activation.

activated voxels, the lowest sensitivity is observed in the “low” magnitude condition, where detection drops to 79.5% with 200 accepted simulations  $n$ . Within this category, the “early–low” case performs worst, reaching only 71.7% accuracy at the same tolerance level. By comparison, the “high” magnitude case consistently yields near-perfect performance, remaining at 100% across most conditions, with only a slight decrease to 99.8% in the “high–early” case at 150 and 200 accepted simulations  $n$ .

For the human smoking dataset, we conducted a proof-of-concept analysis comparing vPET-ABC to lp-ntPET with ENP. In Fig. 4, detected activations are shown as a binary map for the lp-ntPET ENP method (in pink) and as a map of model probability (lp-ntPET versus MRTM) for the vPET-ABC method, with posterior model probability  $> 0.5$  indicating that an activation is more likely than not. In this analysis, we adopted a more conservative strategy than in the simulation study. While  $n = 50$  (out of  $N = 10,000,000$  simulations) achieved the best overall performance, we instead chose  $n = 100$  to prioritize control of false positives while preserving an acceptable false-negative rate (Table III). The results show a wider extent of significant dopamine activation using vPET-ABC than lp-ntPET ENP, suggesting improved sensitivity of vPET-ABC. Furthermore, a substantial fraction of voxels in the vPET-ABC probability map have a probability of 1, indicating a maximal degree of certainty of activation at this tolerance level.

#### D. Human [ $^{18}\text{F}$ ]FDG TB-PET Study

Our vPET-ABC pipeline successfully computed kinetic parameter posterior distributions for all 4.4 million voxels in the TB-PET dataset, within 2 minutes for a single coronal slice and 10 hours for the whole volume using the NCI Gadi cluster [46] with a single NVIDIA V100. This is comparable to our in-house NNLS basis function implementation. The computation time was much faster than the anticipated 36667 hours with b-ntPET [7], 733333 hours with iDDPM deep neural network [12], or 733333 hours with SMC. vPET-ABC has a significant speed advantage over other methods, making it an appealing choice for Bayesian kinetic modeling in large volumes of data.

While the 10 hours computation time is still less than ideal for practical clinical use, it is worth noting a trade-off between estimation quality and computational cost can be easily made by adjusting the simulation size, achieving orders of magnitude speed-up.

As illustrated in Fig. 5, there is good agreement between the vPET-ABC  $K_i$  parametric image and the NNLS  $K_i$  image. In particular, the hyper-metabolic tumor in the right lower lobe of the liver is observed in both images. The Patlak image aligns well with the other  $K_i$  images in the brain, myocardium and liver tumor. However, Patlak underestimates  $K_i$  in other tissues where signal-to-noise is low (e.g. due to low tracer uptake) or the TACs do not comply with the assumption of irreversible kinetics [5].

The vPET-ABC  $K_i$  parametric image also appears to have less voxel to voxel variability than NNLS, likely because the Bayesian formulation regularizes voxelwise inference (via the prior and posterior averaging), reducing noise amplification and yielding more spatially coherent parameter maps that reflect the locally spatial-correlated TACs. For a quantitative measure, after detrending each parametric map by subtracting a heavily smoothed (Gaussian FWHM 40 mm) low-frequency background to remove global spatial gradients, and z-scoring within a common mask, local Moran’s  $I$  differed across maps. The upper-tail clustering ( $q_{75}$ ; the 75th percentile of voxelwise local Moran’s  $I$ ) was highest for vPET-ABC (0.0218), followed by SUV (0.0115), NNLS (0.00848), and Patlak (0.00506). Here larger positive  $I$  indicates stronger local clustering of similar voxel values (greater spatial coherence), values near zero indicate weak local association, and negative values indicate local spatial outliers, while medians were near zero for all methods. Spatial agreement of local autocorrelation structure (Pearson correlation between voxelwise local Moran’s  $I$  maps) was strongest between vPET-ABC  $K_i$  and SUV ( $r = 0.8546$ ), moderate for NNLS  $K_i$  and SUV ( $r = 0.6402$ ), and lowest for Patlak  $K_i$  and SUV ( $r = 0.4805$ ). We used SUV as a semi-quantitative reference because it is the most widely used clinical measure and typically exhibits the expected spatial coherence of reconstructed uptake images under standard preprocessing. Thus, agreement with local autocorrelation patterns in the SUV image provides a pragmatic reference for assessing whether a  $K_i$  estimation method yields spatially plausible parametric maps and preserves SUV-like spatial texture.

## V. CONCLUSIONS AND LIMITATIONS

We have introduced a fully vectorized voxelwise ABC framework for next generation PET kinetic modeling that scales to total-body data and returns voxelwise posteriors, model probabilities, and point estimates without requiring an explicit or differentiable likelihood function. In simulations, posterior means were significantly more accurate than NNLS and posterior distributions closely matched SMC references. For model selection between lp-ntPET and MRTM, vPET-ABC maintained higher sensitivity under high noise at some cost to specificity, whereas NNLS with BIC showed the opposite trade-off with an extremely low sensitivity. In a proof-of-concept smoking dataset, vPET-ABC produced probabilistic

TABLE III  
DETECTION PERFORMANCE FOR 4D PHANTOM vPET-ABC WITH  $N = 10,000,000$

Choice of $n$	Activated voxels	NULL voxels	Activated low	Activated high	Activated early	Activated late	Activated early and low	Activated early and high	Activated late and low	Activated late and high
Detected at $n = 200$	88.80%	99.50%	79.50%	99.80%	85.70%	96.80%	71.70%	99.80%	95.00%	100.00%
Detected at $n = 150$	91.20%	98.50%	84.00%	99.80%	88.50%	98.00%	77.00%	99.80%	97.00%	100.00%
Detected at $n = 100$	93.80%	98.00%	88.50%	100.00%	91.70%	99.20%	83.50%	100.00%	98.70%	100.00%
Detected at $n = 50$	96.80%	96.80%	94.00%	100.00%	95.80%	99.20%	91.70%	100.00%	98.70%	100.00%
Detected at $n = 25$	98.50%	93.00%	97.00%	100.00%	98.00%	99.50%	96.00%	100.00%	99.00%	100.00%
Detected at $n = 15$	99.20%	89.30%	98.50%	100.00%	98.80%	100.00%	97.70%	100.00%	100.00%	100.00%

Detection rates are reported as the percentage of correctly identified voxels for each activation class.

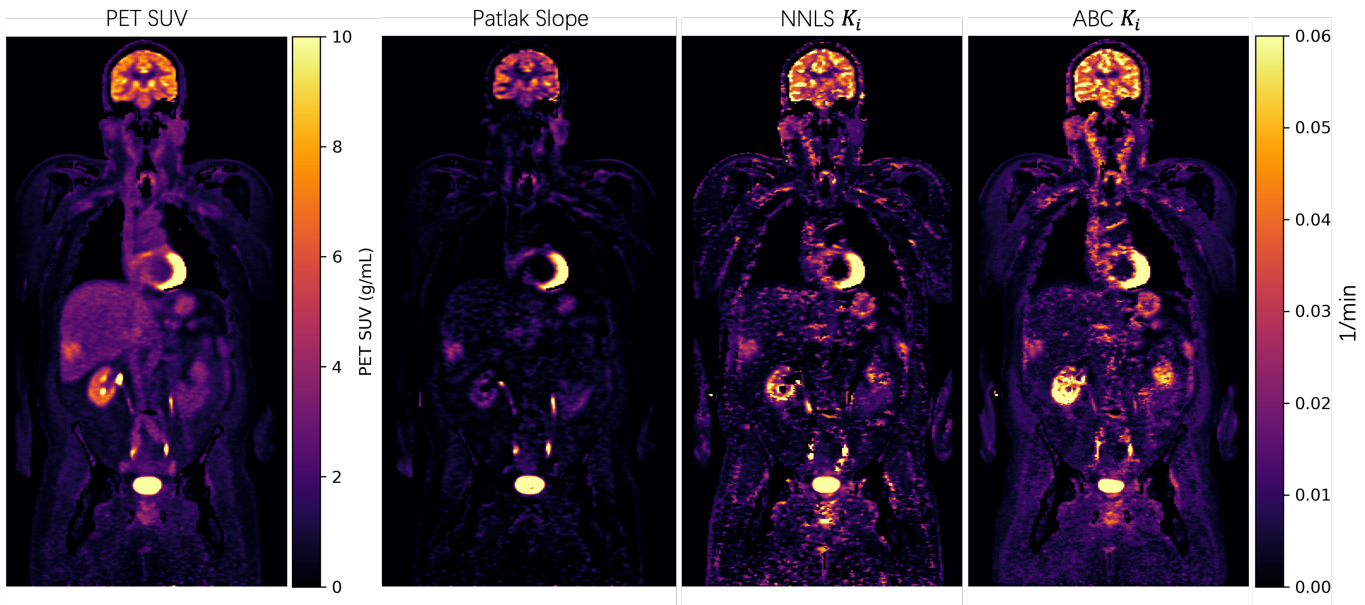


Fig. 5. SUV image (left) and  $K_i$  images obtained using (from left to right): Patlak plot, non linear least squares with non-negativity constraints (NNLS) and vPET-ABC. No post-processing smoothing filter was applied.

maps in broad agreement with lp-ntPET with ENP but with more extensive activation detected, at a conservative tolerance. In a proof-of-concept total-body  $[^{18}\text{F}]\text{FDG}$  dataset, vPET-ABC generated  $K_i$  maps and model probability maps (not shown) in practical runtimes on a single data-center GPU, in good agreement with NNLS. Consistent with this, detrended local Moran's I indicated that vPET-ABC preserved SUV-like local spatial dependence more closely than NNLS and Patlak.

For practical use pipelines we recommend full-TAC summaries and an  $L_1$  distance, with the acceptance proportion selected by a short, tracer-matched pilot. The main engineering constraint is GPU memory, so batching simulations is recommended (automated in our released package), and preprocessing should be consistent between pilot simulations and analysis. A realistic 4D striatal phantom confirmed that tuning the acceptance ratio offers a practical trade-off between sensitivity and specificity across activation magnitude and timing.

Limitations include the approximate nature of ABC posteriors. Future work should account for spatial correlations in the simulation, and benchmark against the latest deep learning kinetic modeling methods [47]. Overall, vPET-ABC provides fast, accurate, training-free likelihood-free Bayesian inference for next-generation PET kinetics with uncertainty

quantification that is practical at the whole-body scale.

#### CODE AVAILABILITY

The `vpet-abc` package is available in <https://github.com/zephyralistair/vPET-ABC-fast-PET-kinetic-modeling-on-large-data/tree/main> and can be installed via `pip`.

#### ACKNOWLEDGMENT

The authors would like to thank Paul Roach, Dale Bailey, Sally Ayesa and Liz Bailey for their advice on protocol design and the nuclear medicine staff at Royal North Shore Hospital for performing the TB-PET studies. We also acknowledge the facilities and the scientific and technical assistance of Sydney Imaging, a core research facility at The University of Sydney, and the National Imaging Facility, a National Collaborative Research Infrastructure Strategy (NCRIS) Capability. This research was also undertaken with the use of the National Computational Infrastructure (NCI Australia) [46]. NCI Australia is enabled by the National Collaborative Research Infrastructure Strategy (NCRIS).

## REFERENCES

- [1] G. Wang, A. Rahmim, and R. N. Gunn, "PET Parametric Imaging: Past, Present, and Future," *IEEE Transactions on Radiation and Plasma Medical Sciences*, vol. 4, no. 6, pp. 663–675, Nov. 2020.
- [2] S. R. Cherry *et al.*, "Total-Body PET: Maximizing Sensitivity to Create New Opportunities for Clinical Research and Patient Care," *Journal of Nuclear Medicine*, vol. 59, no. 1, pp. 3–12, Jan. 2018.
- [3] G. Wang *et al.*, "Total-Body PET Multiparametric Imaging of Cancer Using a Voxelwise Strategy of Compartmental Modeling," *Journal of Nuclear Medicine*, vol. 63, no. 8, pp. 1274–1281, Aug. 2022.
- [4] C. S. Patlak, R. G. Blasberg, and J. D. Fenstermacher, "Graphical evaluation of blood-to-brain transfer constants from multiple-time uptake data," *Journal of Cerebral Blood Flow and Metabolism: Official Journal of the International Society of Cerebral Blood Flow and Metabolism*, vol. 3, no. 1, pp. 1–7, Mar. 1983.
- [5] N. A. Karakatsanis *et al.*, "Generalized whole-body Patlak parametric imaging for enhanced quantification in clinical PET," *Physics in Medicine and Biology*, vol. 60, no. 22, pp. 8643–8673, Nov. 2015.
- [6] R. N. Gunn *et al.*, "Positron Emission Tomography Compartmental Models: A Basis Pursuit Strategy for Kinetic Modeling," *Journal of Cerebral Blood Flow & Metabolism*, vol. 22, no. 12, pp. 1425–1439, Dec. 2002.
- [7] Z. Irace *et al.*, "Bayesian Estimation of the ntPET Model in Single-Scan Competition PET Studies," *Frontiers in Physiology*, vol. 11, May 2020.
- [8] Y. Ke and T. Tian, "Approximate Bayesian Computational Methods for the Inference of Unknown Parameters," in *2017 MATRIX Annals*, J. De Gier, C. E. Praeger, and T. Tao, Eds. Cham: Springer International Publishing, 2019, vol. 2, pp. 515–529.
- [9] M. D. Normandin, W. K. Schiffer, and E. D. Morris, "A linear model for estimation of neurotransmitter response profiles from dynamic PET data," *NeuroImage*, vol. 59, no. 3, pp. 2689–2699, Feb. 2012.
- [10] Y. Fan *et al.*, "PET-ABC: fully Bayesian likelihood-free inference for kinetic models," *Physics in Medicine & Biology*, vol. 66, no. 11, p. 115002, Jun. 2021.
- [11] N. Metropolis *et al.*, "Equation of State Calculations by Fast Computing Machines," *The Journal of Chemical Physics*, vol. 21, no. 6, pp. 1087–1092, Jun. 1953.
- [12] Y. Djebra *et al.*, "Bayesian Posterior Distribution Estimation of Kinetic Parameters in Dynamic Brain PET Using Generative Deep Learning Models," *IEEE Transactions on Medical Imaging*, pp. 1–1, 2025.
- [13] C. Grazian *et al.*, "vPET-ABC: Voxel-wise Approximate Bayesian Inference for Parametric Imaging of Neurotransmitter Release," in *2021 IEEE Nuclear Science Symposium and Medical Imaging Conference (NSS/MIC)*. Piscataway, NJ, USA: IEEE, Oct. 2021, pp. 1–3.
- [14] E. D. Morris *et al.*, "Kinetic Modeling in Positron Emission Tomography."
- [15] —, "Modeling PET Data Acquired During Nonsteady Conditions: What If Brain Conditions Change During the Scan?" *Journal of Nuclear Medicine*, p. jnumed.124.267494, Oct. 2024.
- [16] M. E. Phelps *et al.*, "Tomographic measurement of local cerebral glucose metabolic rate in humans with (F-18)2-fluoro-2-deoxy-D-glucose: Validation of method," *Annals of Neurology*, vol. 6, no. 5, pp. 371–388, Nov. 1979.
- [17] M. Ichise *et al.*, "Linearized Reference Tissue Parametric Imaging Methods: Application to [<sup>11</sup>C]DASB Positron Emission Tomography Studies of the Serotonin Transporter in Human Brain," *Journal of Cerebral Blood Flow & Metabolism*, vol. 23, no. 9, pp. 1096–1112, Sep. 2003.
- [18] D. B. Rubin, "Bayesianly Justifiable and Relevant Frequency Calculations for the Applied Statistician," *The Annals of Statistics*, vol. 12, no. 4, Dec. 1984.
- [19] K. Jonathan *et al.*, "Population growth of human y chromosomes: A study of y chromosome microsatellites," *Molecular biology and evolution*, vol. 16, pp. 1791–8, 01 2000.
- [20] G. Biau, F. Cérou, and A. Guyader, "New insights into Approximate Bayesian Computation," *Ann. Inst. H. Poincaré Probab. Statist.*, vol. 51, no. 1, Feb. 2015.
- [21] Y. Fan *et al.*, "ABC in Nuclear Imaging," Jul. 2016.
- [22] S. Barber, J. Voss, and M. Webster, "The rate of convergence for approximate Bayesian computation," *Electronic Journal of Statistics*, vol. 9, no. 1, Jan. 2015.
- [23] C. Grazian, "Approximate Bayesian Computation with Statistical Distances for Model Selection," Nov. 2025, arXiv:2410.21603 [stat].
- [24] G. Liu *et al.*, "Kinetic metrics of 18 f-fdg in normal human organs identified by systematic dynamic total-body positron emission tomography," *European Journal of Nuclear Medicine and Molecular Imaging*, vol. 48, pp. 2363–2372, 2021.
- [25] H. Sari *et al.*, "First results on kinetic modelling and parametric imaging of dynamic 18f-fdg datasets from a long axial fov pet scanner in oncological patients," *European journal of nuclear medicine and molecular imaging*, vol. 49, no. 6, pp. 1997–2009, 2022.
- [26] D. Feng, S.-C. Huang, and X. Wang, "Models for computer simulation studies of input functions for tracer kinetic modeling with positron emission tomography," *International journal of bio-medical computing*, vol. 32, no. 2, pp. 95–110, 1993.
- [27] E. D. Morris *et al.*, "ntPET: A New Application of PET Imaging for Characterizing the Kinetics of Endogenous Neurotransmitter Release," *Molecular Imaging*, vol. 4, no. 4, p. 7290.2005.05130, Oct. 2005.
- [28] G. I. Angelis *et al.*, "Direct Estimation of Voxel-Wise Neurotransmitter Response Maps From Dynamic PET Data," *IEEE Transactions on Medical Imaging*, vol. 38, no. 6, pp. 1371–1383, Jun. 2019.
- [29] N. Chopin and O. Papaspiliopoulos, *An Introduction to Sequential Monte Carlo*, 1st ed., ser. Springer Series in Statistics. Cham: Springer, 2020.
- [30] M. D. Hoffman and A. Gelman, "The No-U-Turn Sampler: Adaptively Setting Path Lengths in Hamiltonian Monte Carlo," Nov. 2011.
- [31] H. Liu and E. D. Morris, "Detecting and classifying neurotransmitter signals from ultra-high sensitivity PET data: the future of molecular brain imaging," *Physics in Medicine & Biology*, vol. 66, no. 17, p. 175007, Sep. 2021.
- [32] R. F. Muzic and S. Cornelius, "Comkat: Compartment model kinetic analysis tool," *Journal of Nuclear Medicine*, vol. 42, no. 4, pp. 636–645, 2001.
- [33] B. T. Christian *et al.*, "Dynamic PET Denoising with HYPR Processing," *Journal of Nuclear Medicine*, vol. 51, no. 7, pp. 1147–1154, Jul. 2010.
- [34] Y. Zakiniaieiz *et al.*, "Nicotine Patch Alters Patterns of Cigarette Smoking-Induced Dopamine Release: Patterns Relate to Biomarkers Associated With Treatment Response," *Nicotine & Tobacco Research*, vol. 24, no. 10, pp. 1597–1606, Oct. 2022.
- [35] D. Martinez *et al.*, "Imaging human mesolimbic dopamine transmission with positron emission tomography. part ii: Amphetamine-induced dopamine release in the functional subdivisions of the striatum," *Journal of Cerebral Blood Flow & Metabolism*, vol. 23, no. 3, pp. 285–300, 2003.
- [36] H. Liu and E. D. Morris, "Model Comparison Metrics Require Adaptive Correction if Parameters Are Discretized: Proof-of-Concept Applied to Transient Signals in Dynamic PET," *IEEE Transactions on Medical Imaging*, vol. 39, no. 7, pp. 2451–2460, Jul. 2020.
- [37] L. K. S. Sundar *et al.*, "Fully Automated, Semantic Segmentation of Whole-Body<sup>18</sup>F-FDG PET/CT Images Based on Data-Centric Artificial Intelligence," *Journal of Nuclear Medicine*, vol. 63, no. 12, pp. 1941–1948, Dec. 2022.
- [38] T. Yamasaki *et al.*, "First demonstration of in vivo mapping for regional brain monoacylglycerol lipase using PET with [<sup>11</sup>C]SAR127303," *NeuroImage*, vol. 176, pp. 313–320, Aug. 2018.
- [39] S. Bullich *et al.*, "Evaluation of Dosimetry, Quantitative Methods, and Test–Retest Variability of<sup>18</sup>F-PI-2620 PET for the Assessment of Tau Deposits in the Human Brain," *Journal of Nuclear Medicine*, vol. 61, no. 6, pp. 920–927, Jun. 2020.
- [40] H. Tan *et al.*, "Ultralow-dose [18F]FDG PET/CT imaging: demonstration of feasibility in dynamic and static images," *European Radiology*, vol. 33, no. 7, pp. 5017–5027, Jan. 2023.
- [41] L. A. Escobar and B. Skarpness, "The bias of the least squares estimator over interval constraints," *Economics Letters*, vol. 20, no. 4, pp. 331–335, Jan. 1986.
- [42] R. Bro and S. De Jong, "A fast non-negativity-constrained least squares algorithm," *Journal of Chemometrics*, vol. 11, no. 5, pp. 393–401, Sep. 1997.
- [43] S. S. V. Golla *et al.*, "Model selection criteria for dynamic brain PET studies," *EJNMMI Physics*, vol. 4, no. 1, p. 30, Dec. 2017.
- [44] J. E. Cavanaugh and A. A. Neath, "The Akaike information criterion: Background, derivation, properties, application, interpretation, and refinements," *WIREs Computational Statistics*, vol. 11, no. 3, p. e1460, May 2019.
- [45] A. Gelman, J. Hwang, and A. Vehtari, "Understanding predictive information criteria for Bayesian models," *Statistics and Computing*, vol. 24, no. 6, pp. 997–1016, Nov. 2014.
- [46] NCI Australia, "Gadi supercomputer," [Service], 2019. [Online]. Available: <https://doi.org/10.25914/608bfd1838db2>
- [47] Y. Zhao *et al.*, "Generative Consistency Models for Estimation of Kinetic Parametric Image Posteriors in Total-Body PET," Jan. 2026.